RSC Advances

PAPER

View Article Online
View Journal | View Issue



Cite this: *RSC Adv.*, 2023, **13**, 17914

# Vertically aligned $MoS_2$ nanosheets on monodisperse MXene as electrolyte-philic cathodes for zinc ion batteries with enhanced capacity†

Wanting Su,‡ Man Lang,‡ Qingxiao Zhang, Yanan Yang, Huili Li * and Fang Zhang *

Received 10th April 2023
Accepted 29th May 2023

DOI: 10.1039/d3ra02352d

rsc.li/rsc-advances

Zinc ion batteries (ZIBs) have attracted extensive attention for their high safety and environmentally friendly nature, and considerable theoretical capacities. Due to its unique two-dimensional layered structure and high theoretical specific capacities, molybdenum disulfide ($MoS_2$) presents as a promising cathode material for ZIBs. Nevertheless, the low electrical conductivity and poor hydrophilicity of $MoS_2$ limits its wide application in ZIBs. In this work, $MoS_2/Ti_3C_2T_x$ composites are effectively constructed using a one-step hydrothermal method, where two-dimensional $MoS_2$ nanosheets are vertically grown on monodisperse $Ti_3C_2T_x$ MXene layers. Contributing to the high ionic conductivity and good hydrophilicity of $Ti_3C_2T_x$, $MoS_2/Ti_3C_2T_x$ composites possess improved electrolyte-philic and conductive properties, leading to a reduced volume expansion effect of $MoS_2$ and accelerated $Zn^{2+}$ reaction kinetics. As a result, $MoS_2/Ti_3C_2T_x$ composites exhibit high voltage (1.6 V) and excellent discharge specific capacity of 277.8 mA h $g^{-1}$ at 0.1 A $g^{-1}$, as well as cycle stability as cathode materials for ZIBs. This work provides an effective strategy for developing cathode materials with high specific capacity and stable structure.



## Introduction

In recent years, with the rapid development of the economy and increasing energy consumption, high-capacity batteries are highly desired for energy storage purposes.[1–3] In these respects, lithium-ion batteries have been widely used in electronic products and transportation industries due to their high energy density.[1,4,5] However, lithium-ion batteries suffer from the problems of high production cost and intrinsic safety issues. Extensive research has been conducted on metal ion batteries (such as $Mg^{2+}$, $Zn^{2+}$, $Na^{+}$, *etc.*), which are abundant in resources and low cost.[1,6–10] Aqueous zinc ion batteries (ZIBs) are considered to be ideal candidates over lithium-ion batteries due to their low redox potential (−0.763 V *vs.* standard hydrogen electrode (SHE)),[6,11–13] high theoretical specific capacity (820 mA h $g^{-1}$ and 5855 mA h $cm^{-3}$),[14,15] non-toxic properties[6] and abundant Zn resources.[7] A typical ZIB generally compose of Zn metal anode, electrolyte, and cathode electrode for accommodating Zn ions.[16] Except for the most common anode material of zinc metal in ZIBs, battery capacities are more limited by cathodes than anodes. With regards to the cathode materials, extensively investigated active materials include manganese-based materials, vanadium-based materials, Prussian blue analogs, and organic electrode materials and so on.[17–21] However, the electrochemical and physical properties of these active materials are still inadequate to achieve high-performance ZIBs.[22] It is urgent to develop cathode materials for ZIBs with high specific capacity and stable structures for large-scale commercial applications.[23,24]

Molybdenum disulfide ($MoS_2$), a representative transition metal dichalcogenide, possesses the two-dimensional (2D) layered structure similar to graphite.[25–27] The $MoS_2$ is considered as promising host material for ion intercalation due to the unique layered structure bonded by weak van der Waals' forces.[2,28,29] These characteristics indicate that the layered materials $MoS_2$ demonstrate extraordinary potential as electrode materials for ZIBs.[30,31] However, the low intrinsic conductivity, poor structural stability, and severe self-stacking of $MoS_2$ hinder its wide application of $MoS_2$ in zinc storage materials.[2] In addition, the larger hydrated ionic diameter of $Zn^{2+}$ (approximately 0.86 nm) and strong electrostatic interactions with $MoS_2$ result in sluggish reaction kinetics and difficultly reversible $Zn^{2+}$ intercalation.[15,32–34] To alleviate these problems, several modification methods have been proposed to improve the electrochemical performance of ZIBs using $MoS_2$, including the introduction of sulfur defects,[35] partial replacement of sulfur atoms by oxygen atoms,[36] modulation of

*Key Laboratory of Resource Chemistry, Joint International Research Laboratory of Resource Chemistry, Ministry of Education, College of Chemistry and Materials Science, Shanghai Normal University, Shanghai 200234, China. E-mail: li_huili@shnu.edu.cn; zhangfang@shnu.edu.cn*

† Electronic supplementary information (ESI) available. See DOI: https://doi.org/10.1039/d3ra02352d

‡ Wanting Su and Man Lang contributed equally to this work.

phases,[33] and expansion of layer spacing.[37] For instance, Wang preferentially inserted Zn ions into sulfur vacancies building defect engineered $MoS_{2-x}$ nanosheets.[35] The ZIBs based on $MoS_{2-x}$ nanosheets exhibited discharge specific capacity of 138.6 mA h $g^{-1}$ at 0.1 A $g^{-1}$. In another work, molecular engineering in terms of structure defects manufacturing and O-doping on $MoS_2$ was reported by Li to expand the interlayer spacing (from 6.2 to 9.6 Å).[26] Therefore, the tailored $MoS_2$–O cathode respectively displayed specific capacity of 261 mA h $g^{-1}$ at 0.1 A $g^{-1}$ with 102.4 mA h $g^{-1}$ at 10 A $g^{-1}$, indicating unprecedentedly high rate-capability. In addition, due to metallic 1 T $MoS_2$ with better electronic conductivity comparable than 2H $MoS_2$, vertically aligned 1 T phase $MoS_2$ nanosheet array on carbon cloth were fabricated to improve capacities.[33] As a result, the free-standing cathode exhibited excellent specific capacity of 198 mA h $g^{-1}$ at current density of 0.1 A $g^{-1}$. Most recently, $MoS_2$/polyaniline (PANI) hybrid with inter-overlapped heterostructure was explored with expanded interlayer spacing as large as 1.03 nm of (002) plane in the $MoS_2$/PANI hybrid.[37] The $MoS_2$/PANI hybrid delivered high reversible capacity of 106.5 mA h $g^{-1}$ at a current density of 1.0 A $g^{-1}$. Nonetheless, the conductivity, swelling effect and self-aggregation phenomenon still need to be further improved to obtain high capacity and stable cycling ZIBs.

$Ti_3C_2T_x$ MXene, typical 2D transition metal carbonitride, exhibits excellent properties, such as abundant surface groups,[38] tunable interlayer spacing,[39] excellent electrical conductivity[40] and good hydrophilicity.[41] $Ti_3C_2T_x$ MXene has been widely developed and investigated for energy storage. Herein, the $MoS_2/Ti_3C_2T_x$ composites were constructed through the 2D $MoS_2$ nanosheets vertically aligned on 2D $Ti_3C_2T_x$ MXene by a one-step hydrothermal method. The resulting 3D open network architecture of the $MoS_2/Ti_3C_2T_x$ composites increased the interfacial contact with the electrolyte and shortened the diffusion pathways for $Zn^{2+}$. Due to the high electrical conductivity and hydrophilicity of monodisperse $Ti_3C_2T_x$ MXene, the introducing of $Ti_3C_2T_x$ suppressed self-stacking of $MoS_2$ nanosheets, accelerated the migration rate of $Zn^{2+}$ and enhanced the reaction kinetic rate. Impressively, the as-fabricated $MoS_2/Ti_3C_2T_x$ composites exhibited high voltage to 1.6 V, high discharge specific capacity of 277.8 mA h $g^{-1}$ at 0.1 A $g^{-1}$ and 80% capacity retention after 5000 cycles when the current density was 10.0 A $g^{-1}$. In addition, the intercalation/deintercalation mechanism and kinetic diffusion process of Zn ion diffusion were demonstrated using *ex situ* X-ray diffraction (ex-XRD), X-ray photoelectron spectroscopy (XPS) and galvanostatic intermittent titration technique (GITT). This work presented new insights on the application of layered materials as high-performance cathodes for ZIBs.

# Experimental

### Synthesis of $Ti_3C_2T_x$ MXene

As previously reported, $Ti_3C_2T_x$ was obtained after selective etching of the Al layer from $Ti_3AlC_2$ feedstock.[42,43] First, 3.2 g LiF was dissolved in 40 mL HCl (9 mol $L^{-1}$), stirred for five minutes and then 2 g $Ti_3AlC_2$ was slowly added to the above solution and the mixed solution was stirred at 35 °C for 24 h. The obtained mixed solution was washed with deionized water by centrifugation to a supernatant with pH of approximately 6, and the precipitate was sonicated with an appropriate amount of deionized water under argon for 1 h. Finally, the $Ti_3C_2T_x$ dispersion was centrifuged at 3500 rpm for 20 min to obtain $Ti_3C_2T_x$ dispersion.

### Synthesis of $MoS_2/Ti_3C_2T_x$ MXene composites

In brief, 0.3 mmol ammonium molybdate and 13.1 mmol thiourea were dissolved in 50 mL water, and then 10 mg $Ti_3C_2T_x$ (5 mg $mL^{-1}$) was added to the mixed solution, which was stirred for 15 min at room temperature and sonicated for 5 min. The mixed solution was transferred to Teflon stainless steel kettles and reacted at 200 °C for 24 h. The resulting product was then washed three times with deionized water and freeze-dried for two days. In contrast, $MoS_2$ nanosheets were synthesized without the addition of $Ti_3C_2T_x$. All the materials were used directly for electrochemical experiments without further purification.

### Characterization methods

XRD were obtained using a Rigaku D/Max B diffractometer with Cu-Kα radiation. The morphology and microstructure of the samples were observed by field emission scanning electron microscopy (SEM, HITACHI, S-4800) and transmission electron microscopy (TEM, JEOL JEM-2100), respectively. XPS were measured by using Thermo Scientific Nexsa system to analysis the chemical composition of the material surface. The atomic force microscope (AFM) tested the sheet thickness of $Ti_3C_2T_x$ MXene using Bruker Dimension Icon. The specific surface area was tested with Tri Star II 3020 by Michael Corporation, USA. Raman spectroscopy were performed with a DXRZXi model (Thermo, USA).

### Electrochemical characterizations

Electrochemical performance tests were performed in a CR2032 coin cell with $MoS_2/Ti_3C_2T_x$ as the cathode, 0.1 mm zinc foil as the anode, 21 mol $L^{-1}$ lithium bis(trifluoromethane sulfonyl) imide salt (LiTFSI, Innochem, 98%) and 1 mol $L^{-1}$ $Zn(CF_3SO_3)_2$ (TCI, >98%) as the electrolyte, and a glass fiber filter membrane (Whatman, GF/D) as the septum. The $MoS_2/Ti_3C_2T_x$ cathode was prepared by first grinding the active material, carbon black, and polyvinylidene fluoride (PVDF, Kejing Co. Shenzhen) in a 7 : 2 : 1 ratio in a mortar and pestle for thirty minutes, then pouring the solid powder into a small glass vial and adding an appropriate amount of *N*-methylpyrrolidone (NMP, Aladdin, >99%) solvent and stirring for 6 h. Finally, the mixed slurry was evenly coated on the titanium foil substrate and dried under vacuum at 80 °C for 12 h. The dried poles were cut into $\Phi = 12$ mm discs, and the average active substance loading of the prepared cathodes was 1.0–1.5 mg $cm^{-2}$. The cell multiplicity performance, cycling performance and GITT tests were carried out with the LAND 2001A cell test system in the voltage range of 0–1.6 V. Cyclic voltammetry (CV), electrochemical impedance spectrogram (EIS), and galvanostatic charge/discharge (GCD) were tested

using the same electrochemical workstation (CHI 760E, C&H Co., Shanghai, China), and the frequency range of EIS spectrogram was $10^{-2}$–$10^{5}$. The above tests were performed at room temperature.

## Results and discussion

### Synthesis and characterization of $MoS_2/Ti_3C_2T_x$ composites

The $MoS_2/Ti_3C_2T_x$ MXene composites were synthesized *via* hydro-thermal reaction of $(NH_4)_6Mo_7O_{24}\cdot 4H_2O$ and $NH_2CSNH_2$ in presence of $Ti_3C_2T_x$ MXene as illustrated in Fig. 1a. Prior to the hydro-thermal reaction, homogeneous single-layer $Ti_3C_2T_x$ MXene dispersions with thickness of 2.2 nm (Fig. S1 and S2a†) were obtained through LiF and HCl etching of $Ti_3AlC_2$ MAX (Fig. S2b†), followed by ultrasonic process. The Raman spectra (Fig. 1b) and XRD patterns (Fig. S3–S4†) were recorded to understand the characteristic of $MoS_2/Ti_3C_2T_x$ MXene composites. According to the XRD pattern, the characteristic peaks of the (002) plane at 2θ values of 9.6° for $Ti_3AlC_2$ MAX shifted to 7.2° for $Ti_3C_2T_x$ MXene, which was remarkedly shifted to 10.0° of $MoS_2/Ti_3C_2T_x$ MXene (Fig. S3†). In comparison to pure $MoS_2$, the diffraction peak at the (002) plane of $MoS_2/Ti_3C_2T_x$ MXene was slightly shifted from 13.6° to 12.6°. Based on the Bragg's equation ($n\lambda = 2d\sin\theta$), the interlayer spacing of $MoS_2$ was modified 0.65 nm of pure $MoS_2$ from to 0.70 nm in the $MoS_2/Ti_3C_2T_x$ MXene composites. Furthermore, the characteristic peaks at 143.1 $cm^{-1}$ ($J_1$), 232.6 $cm^{-1}$ ($J_2$), and 332.5 $cm^{-1}$ ($J_3$) demonstrated the successful construction of dominating 1T $MoS_2$ in heterostructure $MoS_2/Ti_3C_2T_x$ MXene (Fig. 1b). The peak located at 278.2 $cm^{-1}$ was assigned to the $E_{1g}$ characteristic vibration of Mo in octahedral coordination, where the surface metal Mo atoms were connected to S atoms.

The chemical composition and valence states of $MoS_2/Ti_3C_2T_x$ MXene composite were further analyzed using XPS spectra. The presence of Mo, S, Ti, C and O elements were confirmed in $MoS_2/Ti_3C_2T_x$ MXene composites (Fig. S5a†). In Ti 2p spectrum (Fig. S5b†), the signals at 458.3 and 463.7 eV were identified as the $2p_{3/2}$ and $2p_{1/2}$ orbits of $Ti^{3+}$ in $Ti_3C_2T_x$ MXene, respectively. The absence of $2p_{3/2}$ and $2p_{1/2}$ doublet at 458.7 and 464.6 eV indicated the absence of the Ti–O bonds in $Ti_3C_2T_x$ MXene and surface-attached oxygen containing groups. Deposited in high-resolution S 2p spectrum (Fig. 1c), the S $2p_{3/2}$ and S $2p_{1/2}$ spectra were also deconvoluted into 1T and 2H phases. The peaks at binding energies of 162.6 eV and 163.9 eV were severally assigned to S $2p_{1/2}$ and S $2p_{3/2}$ of 1T phases, indicating the presence of divalent sulfur ions. The $Mo^{6+}$ $3d_{3/2}$, $Mo^{4+}$ $3d_{3/2}$ and $Mo^{4+}$ $3d_{5/2}$ of 1T phases were characterized at 236.5 eV, 232.3 eV and 229.2 eV, respectively (Fig. 1d). The Mo in hierarchical structure of $MoS_2/Ti_3C_2T_x$ MXene composites were dominant in $Mo^{4+}$ and minimal in the oxidization of $Mo^{6+}$. Furthermore, different from the commercial $MoS_2$ dominant in 2H phases (Fig. S6†), the $MoS_2/Ti_3C_2T_x$ MXene composites mainly consisted of 1T phase (about 66%), which was consistent with Raman spectra (Fig. 1b).

The morphology and structure of $MoS_2/Ti_3C_2T_x$ MXene composites were characterized using Scanning Electron Microscope (SEM), Energy Dispersive X-ray Spectroscopy (EDX) and Transmission Electron Microscope (TEM). The $MoS_2/Ti_3C_2T_x$ MXene composites exhibited flower-like structures with evident wrinkles and corrugations (Fig. 2a–c). Due to the

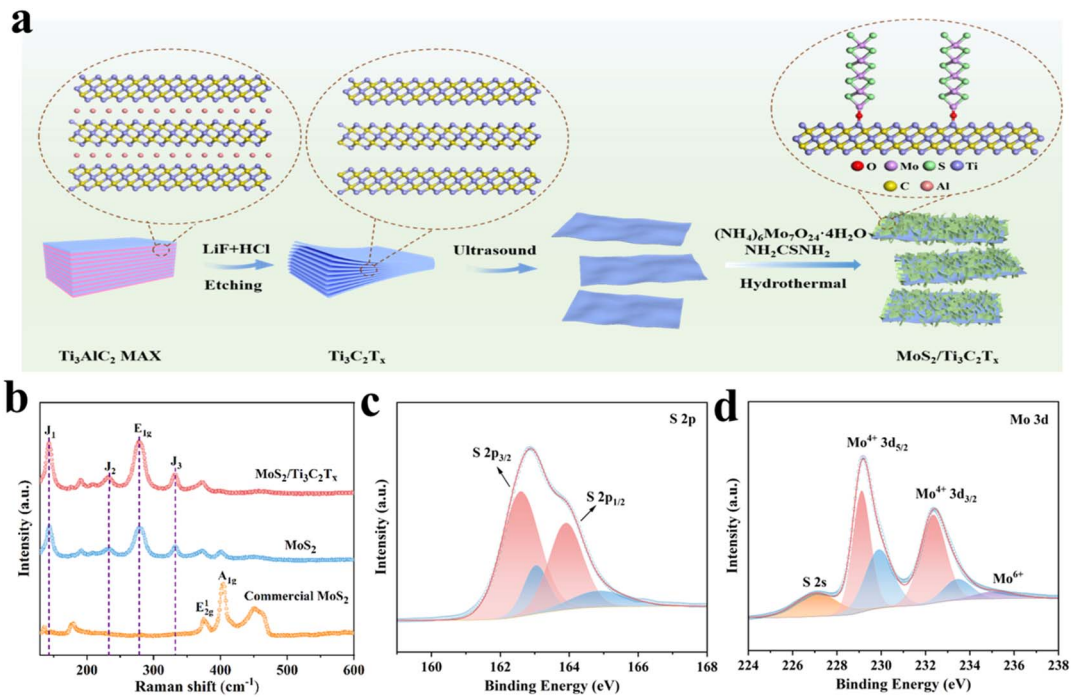


Fig. 1 (a) Schematic synthesis of the $MoS_2/Ti_3C_2T_x$ composites. (b) Raman spectra of commercial $MoS_2$, pure $MoS_2$ and $MoS_2/Ti_3C_2T_x$ composites. Detailed XPS spectra of (c) S 2p and (d) Mo 3d.

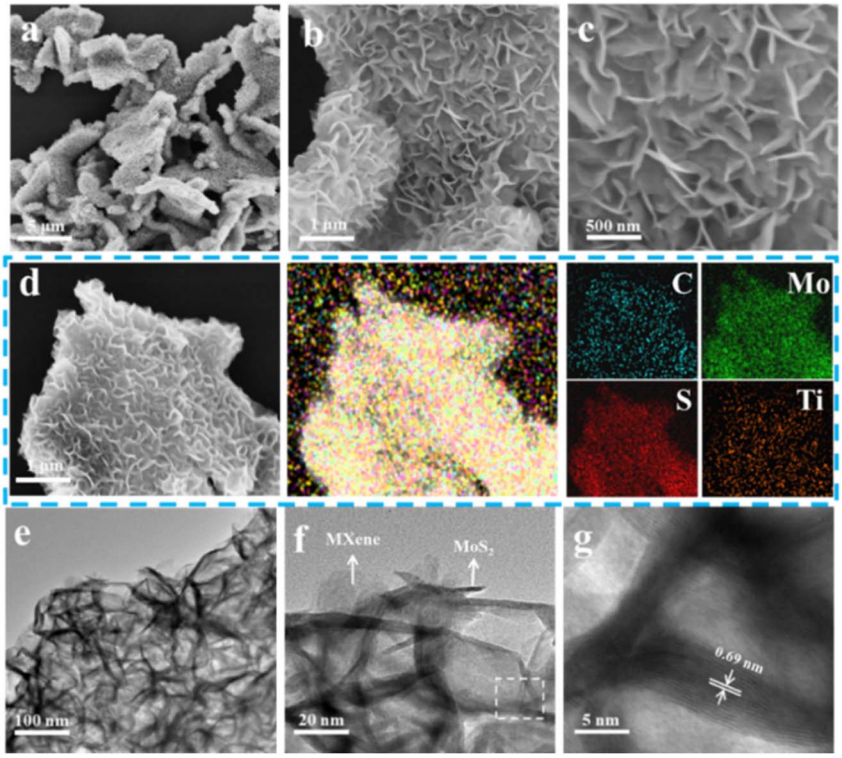


Fig. 2 (a–c) SEM images, (d) element mapping and (e–g) TEM images of $MoS_2/Ti_3C_2T_x$ MXene composites.

existence of $Ti_3C_2T_x$ MXene skeleton, heterogeneous nucleation avoided the agglomeration of $MoS_2$ nanosheets. Moreover, MoS2 nanosheets were vertically aligned on the $Ti_3C_2T_x$ MXene surface, displaying uniform distribution of C, Mo, S and Ti elements (Fig. 2d). The hierarchical structure of $MoS_2$ nanosheets on the highly conductive $Ti_3C_2T_x$ MXene substrate facilitated fast electron transfer and easy penetration of the electrolyte, resulting in considerable electrochemical properties. Furthermore, the staggered $MoS_2$ nanosheets with low stacking height, providing lowered the $Zn^{2+}$ migration potential barrier, provided more active sites for the intercalation of zinc ions.[44] As elucidated in Fig. 2e–g, the fabricated $MoS_2$ nanosheets exhibited the slightly modified interlayer spacing of 0.7 nm compared to commercial 2H $MoS_2$ (0.65 nm, Fig. S7†), which was well in accordance with XRD data (Fig. 1b). Due to the reduced ion diffusion resistance and energy barrier, the enlarged interlayer spacing accelerated the reaction kinetics of $Zn^{2+}$ for $MoS_2/Ti_3C_2T_x$ MXene composites.

### Electrochemical performance of $MoS_2/Ti_3C_2T_x$ composites for ZIBs

$Zn//MoS_2/Ti_3C_2T_x$ MXene batteries were constructed utilizing $MoS_2/Ti_3C_2T_x$ MXene as cathode and zinc as anode with electrolyte consisted of 21 mol $L^{-1}$ LiTFSI and 1 mol $L^{-1}$ $Zn(CF_3SO_3)_2$, respectively (Fig. 3a). The electrochemical performance of $MoS_2/Ti_3C_2T_x$ MXene composites was investigated through GCD and rate capability of $Zn//MoS_2/Ti_3C_2T_x$ MXene batteries between 0 V and 1.6 V as demonstrated in Fig. 3b and c. $Zn//MoS_2/Ti_3C_2T_x$ batteries displayed specific discharge capacities of 277.8, 228.5, 175.6, 138.9 and 106.4 mA h $g^{-1}$ at current densities of 0.1, 0.2, 0.5, 1.0, and 2.0 A $g^{-1}$, respectively. The specific discharge capacities were found to be higher than that of $MoS_2$ (Fig. 3c and S8†), $MoS_2$ with 1 mol $L^{-1}$ $Zn(CF_3SO_3)_2$ electrolyte (Fig. S9†) and other $MoS_2$-based ZIBs as presented in Fig. 3d and Table S1.†[31–35,37,45–53] This was mainly attributed to the increased specific surface area of $MoS_2/Ti_3C_2T_x$ MXene composites in Fig. S10.† When the current density returned to 0.1 A $g^{-1}$, the corresponding discharge capacity recovered to approximately 233.0 mA h $g^{-1}$ maintaining about 84% of the original discharge capacity. This indicated the good electrochemical reversibility and fast reaction kinetics of the prepared ZIBs. Furthermore, the prepared ZIBs using $MoS_2/Ti_3C_2T_x$ MXene composites exhibited a power density of 37.7 W $kg^{-1}$ and an energy density of 108.3 W h $kg^{-1}$. Ascribing to the introduction of $Ti_3C_2T_x$ MXene, the vertically aligned heterostructure with expanded interlayer spacing and good electrolyte-philic properties (Fig. S11†) of $MoS_2$ generated the considerable electrochemical properties.

From the EIS spectra in Fig. 3e, Nyquist diagram possessed a semicircle in the high-frequency region and a diagonal line in the low-frequency region. The intercept on the real axis and diameter of the semicircle reflected the equivalent series resistance ($R_e$) and the charge-transfer resistance ($R_{ct}$), respectively.[54] The slope of diagonal line in the low-frequency region indicates Warburg resistance ($Z_w$) caused by ion diffusion in the electrode. The $Zn//MoS_2/Ti_3C_2T_x$ batteries displayed smaller $R_{ct}$ (31.1 Ω) than that of $Zn//MoS_2$ batteries (114.7 Ω), attributed to the high conductivity and reduced the zinc ions intercalation energy barrier of the 2D/2D $MoS_2/Ti_3C_2T_x$ heterostructure. Furthermore, $MoS_2/Ti_3C_2T_x$ composites exhibited decreased $Z_w$

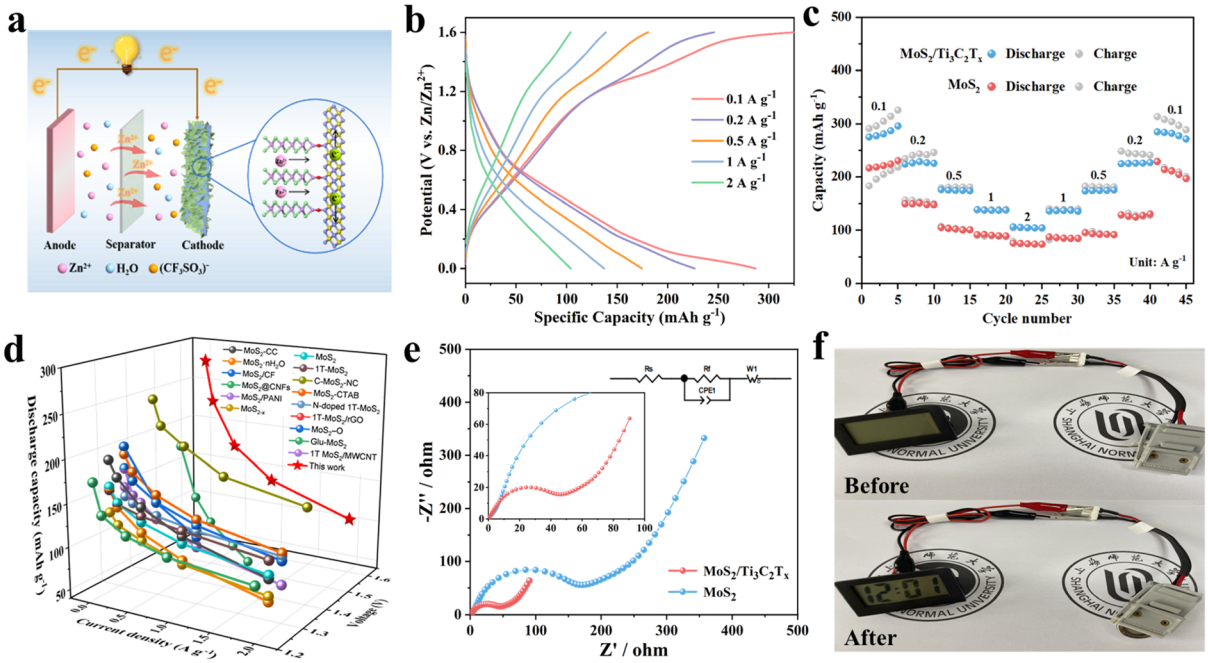


Fig. 3 Electrochemical performances of Zn//$MoS_2/Ti_3C_2T_x$ MXene batteries in 21 mol $L^{-1}$ LiTFSI and 1 mol $L^{-1}$ $Zn(CF_3SO_3)_2$ aqueous electrolyte. (a) Schematics of the mechanism of Zn//$MoS_2/Ti_3C_2T_x$ MXene battery. (b) The galvanotactic charge/discharge curves and (c) rate capability of Zn//$MoS_2/Ti_3C_2T_x$ MXene batteries under various current densities. (d) Discharge capacity of ZIBs compared with the values reported of other $MoS_2$ based ZIBs. (e) Electrochemical impedance spectroscopy spectra of Zn//$MoS_2/Ti_3C_2T_x$ and Zn//$MoS_2$ batteries. Inset: the partial enlargement EIS at the high frequency region. (f) Digital photographs of Zn//$MoS_2/Ti_3C_2T_x$ MXene batteries to power a lock.

compared to $MoS_2$ and commercial $MoS_2$, signifying the faster diffusion rate of $Zn^{2+}$ and improved ion conductivity with introduction of conductive $Ti_3C_2T_x$ in Fig. S12.† Remarkably, an exceptionally long lifetime of 5000 cycles was obtained with stable capacity retention of over 80% when cycled at high current density of 10.0 A $g^{-1}$ (Fig. S13†), better than that of Zn//$MoS_2$ batteries using 1 mol $L^{-1}$ $Zn(CF_3SO_3)_2$ electrolyte (Fig. S14†). The $MoS_2/Ti_3C_2T_x$ MXene heterostructure structure with expanded layer spacing was conducive to intercalation/delamination of zinc ion. The morphologies of $MoS_2/Ti_3C_2T_x$ MXene nanosheets were well preserved without amount of aggregation after cycling measurements (Fig. S15†). Furthermore, the interlayer spacing of $MoS_2/Ti_3C_2T_x$ MXene composites well maintained with obvious lattice fringes after long-term cycle test (Fig. S16†). Moreover, at low current density of 1.0 A $g^{-1}$, capacity can be maintained about 80% of initial capacity after 800 charge/discharge cycles (Fig. S17†), indicating excellent structural stability for ZIB. In order to explore the practical application value of ZIBs, one Zn//$MoS_2/Ti_3C_2T_x$ MXene ZIB can illuminate a clock (Fig. 3f), revealing that the prepared ZIBs can be used as electrochemical storage device to applied other electronic products.

### Kinetics of Zn//$MoS_2/Ti_3C_2T_x$ ZIBs

The CV curve was obtained at different sweep rates within the voltage window of 0–1.6 V *vs.* $Zn/Zn^{2+}$ in Fig. 4a. With the increase of scanning rate from 0.4 mV $s^{-1}$ to 1.2 mV $s^{-1}$, the area of the CV curve gradually increased along with obviously enhancement in current intensity of the redox peak. This was because the diffusion resistance increased with the increase of sweep rate. At scanning rate of 0.1 mV $s^{-1}$, the couple cathode peak and anode peak severally represented at 0.27 V and 1.25 V, in accordance with the discharge and charge plateaus in GCD curves (Fig. 3b), corresponding to insertion/desertion of zinc ions. Based on the CV curves obtained at various rates, electrochemical kinetic processes of Zn//$MoS_2/Ti_3C_2T_x$ batteries can be determined by the following relation:

$$i = av^b$$

where $a$ and $b$ were variable parameters, $i$ and $v$ represented peak current and the corresponding scan rate, respectively. In general, while the co-efficient $b$ value equaled to 1 or 0.5, the electrochemical process was dominated by capacitive-limited controlled behavior or diffusion-limited processes, respectively. From the slope fitting curves in Fig. 4b, the $b$ values of peaks 1 and 2 were separately calculated as 0.80 and 0.88, revealing that capacitive-limited process and diffusion-controlled behavior synergistically dominated the charge storage process of $MoS_2/Ti_3C_2T_x$ composites. Moreover, the capacitive ($k_1v$) contribution and diffusion ($k_2v^{1/2}$) contribution of $MoS_2/Ti_3C_2T_x$ composites can be further rationally quantified by the following equation:

$$i = k_1v + k_2v^{1/2}$$

where $k_1$ and $k_2$ were parameters changed with the peak current ($i$). Fig. 4c illustrated the ratio of the capacitive contribution (blue) to the diffusion contribution (red) as a function of scan

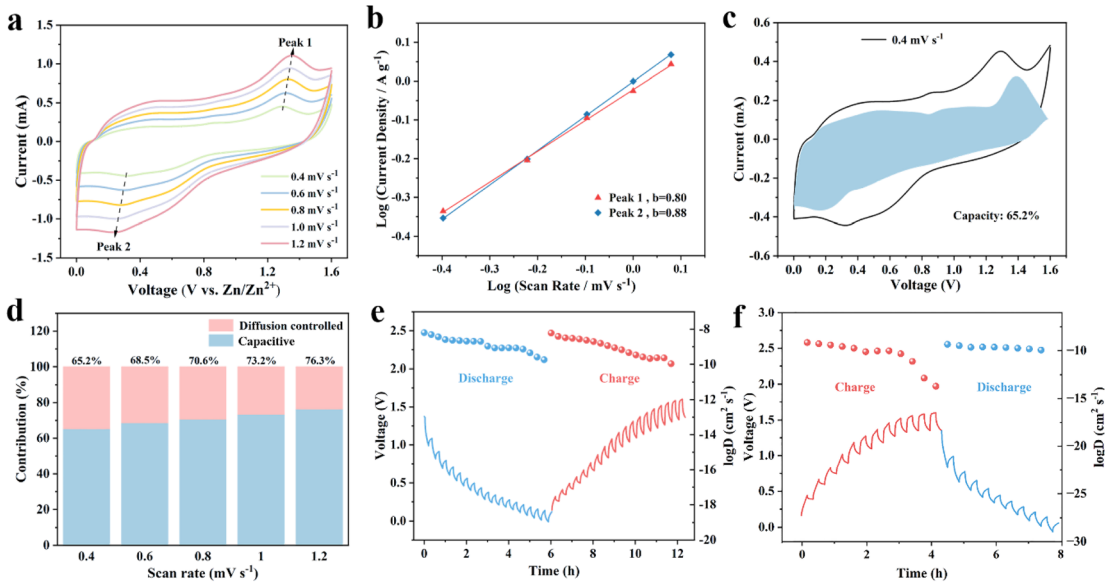


Fig. 4 (a) Cyclic voltammogram profiles of Zn//$MoS_2$/$Ti_3C_2T_x$ batteries at various scan rates. (b) The fitting plots between log(*i*) and log(*v*) at various peak currents. (c) Quantification of the capacitive (blue area) and diffusion charge storage in the $MoS_2$/$Ti_3C_2T_x$ electrode at a scan rate of 0.4 mV $s^{-1}$ and (d) the ratio of the capacitive contribution (blue) to the diffusion contribution (red) as a function of scan rate. Charge/discharge GITT curves and corresponding $Zn^{2+}$ diffusion coefficients for (e) $MoS_2$/$Ti_3C_2T_x$ and (f) $MoS_2$ at 0.5 A $g^{-1}$.

rate. The value of capacitive contribution exhibited nearly 65.2% at the scan rate of 0.4 mV $s^{-1}$ (Fig. 4d). This value steadily increased with increasing scan rates due to the slower lower capacitive-limited process compared to diffusion-controlled behavior.

The kinetics of $Zn^{2+}$ intercalation during the charge/discharge reaction of $MoS_2$/$Ti_3C_2T_x$ cathode material was studied in depth using the GITT. The diffusion coefficient of $Zn^{2+}$ ($D_{Zn^{2+}}$) was calculated using the following equation:

$$D_{Zn^{2+}} = \frac{4}{\pi\tau}\left(\frac{mV_m}{MA}\right)^2\left(\frac{\Delta E_s}{\Delta E_\tau}\right)^2$$

where the variables $\tau$, $M$, $m$, $V_m$ and $A$ severally represented the relaxation time, molar mass of active material, mass of active material, molar volume, and the contact area between electrode and electrolyte. Additionally, $\Delta E_s$ and $\Delta E_\tau$ represented the pulse voltage change and voltage change of constant-current charge/discharge, respectively. In the voltage range of 0–1.6 V, the ($D_{Zn^{2+}}$) of $MoS_2$/$Ti_3C_2T_x$ MXene ZIBs were calculated to be in the range of $10^{-8}$ to $10^{-10}$ $cm^2$ $s^{-1}$ (Fig. 4e), which was superior to that of $MoS_2$ ($10^{-9}$ to $10^{-14}$ $cm^2$ $s^{-1}$, Fig. 4f), and other previously reported modified-$MoS_2$ electrode materials ($10^{-10}$ to $10^{-14}$ $cm^2$ $s^{-1}$).[32,45] The improved performance of the Zn//$MoS_2$/$Ti_3C_2T_x$ MXene ZIBs can be attributed to the introduction of $Ti_3C_2T_x$ into $MoS_2$, which increased the contact area, shortened the transport distance of $Zn^{2+}$ and generated the accelerated migration rate of $Zn^{2+}$. The increase of charge transfer rate and the rapid diffusion of $Zn^{2+}$ ensured the excellent rate performance and cycle stability of the Zn//$MoS_2$/$Ti_3C_2T_x$ MXene ZIBs.

### Mechanism of Zn//$MoS_2$/$Ti_3C_2T_x$ ZIBs

*Ex situ* XRD characterization and XPS measurements were performed to investigate the Zn storage mechanism of $MoS_2$/$Ti_3C_2T_x$ electrode. Specifically, the charge–discharge marked states (points A–G) were selected for *ex situ* XRD testing (Fig. 5a), focusing on the structural evolution of $MoS_2$/$Ti_3C_2T_x$ electrode. During the discharge process (A–D), the (002) characteristic peak of $MoS_2$/$Ti_3C_2T_x$ electrode shifted to the lower angle, demonstrating that the insertion of $Zn^{2+}$ ions with expanding the layer spacing of $MoS_2$/$Ti_3C_2T_x$ electrode. After charging (D–G), the (002) peak position returned to the original point A, which was caused by the desertion of $Zn^{2+}$ ions from the $MoS_2$/$Ti_3C_2T_x$ electrode. The charge/discharge process was consistent with the CV curves (Fig. 4a). The results indicated that the structure of $MoS_2$/$Ti_3C_2T_x$ possessed good reversibility without collapsing during the ion embedding-detachment process.

The reversible insertion/extraction mechanism of $Zn^{2+}$ was also confirmed through XPS measurements (Fig. 5b and c). As expected, no diffraction signal of Zn 2p was detected in the pristine condition. Nevertheless, two remarkable diffraction peaks were observed at 1045.8 eV and 1022.7 eV while discharged, corresponding to Zn $2p_{1/2}$ and Zn $2p_{3/2}$. The diffraction peak indicated the insertion of $Zn^{2+}$ to the $MoS_2$/$Ti_3C_2T_x$ electrode and the adsorption of $Zn^{2+}$ in the electrolyte due to the capacitive behavior in consistent with the *b* value in CV measurement (Fig. 4d). Upon reverse charging, the inserted portion of $Zn^{2+}$ disappeared from the diffraction peak but the adsorbent portion remained, indicating the reversible insertion/extraction of $Zn^{2+}$. The effect of $Zn^{2+}$ on the valence changes of Mo elements can be evidenced in the *ex situ* XPS patterns (Fig. 5c). With the insertion of $Zn^{2+}$ at discharged state, the S 2s peak shifted by about 0.2 V to the lower binding energy and the intensity of $Mo^{6+}$ was aggressively enhanced. Conversely, the S 2s peak returned to its original state and the intensity of $Mo^{6+}$ significantly decreased at the discharged state. These results confirmed the zinc storage mechanism of $MoS_2$/

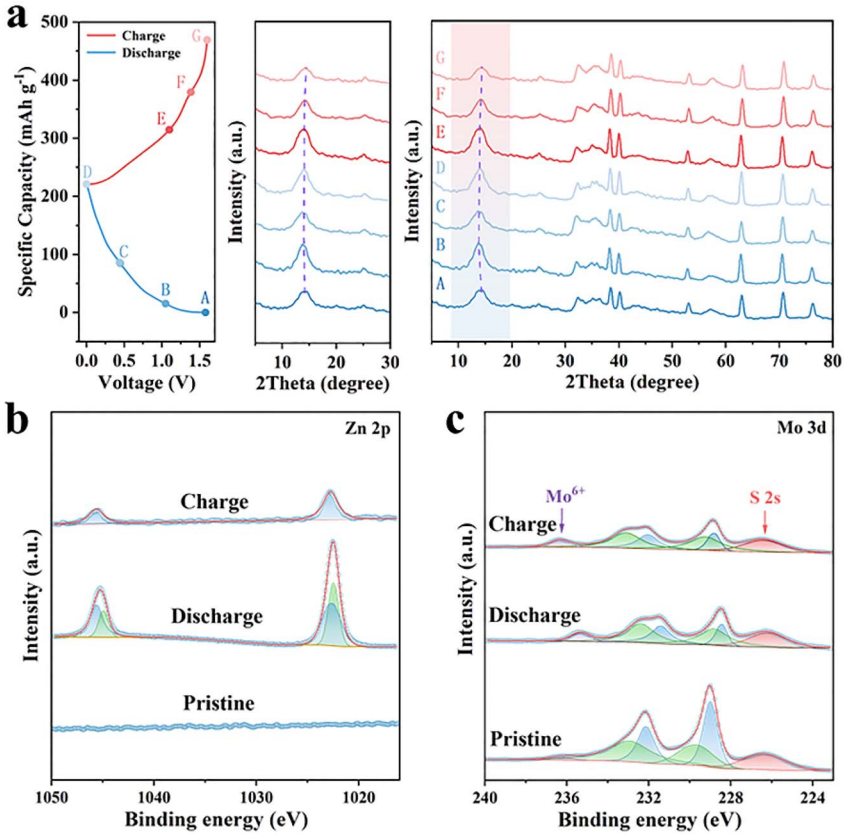


Fig. 5 Zn-storage mechanism of $MoS_2/Ti_3C_2T_x$ composites. (a) Charge/discharge profiles of Zn//$MoS_2/Ti_3C_2T_x$ battery at a current density of 0.1 A $g^{-1}$. The *ex situ* XRD patterns collected at different charge/discharge depths. The *ex situ* high-resolution XPS spectroscopy of (b) Zn 2p and (c) Mo 3d at different charge/discharge depths.

$Ti_3C_2T_x$ electrode which agreed well with the *ex situ* XRD results (Fig. 5a).

As mentioned above, it can be calculated that 0.83 $Zn^{2+}$ can be inserted into per molecule of $MoS_2$ at the current density of 0.1 A $g^{-1}$. Consequently, the electrochemical mechanism of the $MoS_2/Ti_3C_2T_x$ battery can be illustrated and formulated as following:

$$\text{Cathode: } 0.83Zn^{2+} + 1.66e^- + MoS_2 \leftrightarrow Zn_{0.83}MoS_2$$

$$\text{Anode: } Zn^{2+} + 2e^- \leftrightarrow Zn$$

During the discharged process, Zn anode lost the electron to be reduced to $Zn^{2+}$. Simultaneously, $Zn^{2+}$ ions were intercalated into the $MoS_2$ to establish the phase of $Zn_{0.83}MoS_2$ at the cathode. During the reverse charging, $Zn^{2+}$ ions were gradually extracted from $Zn_{0.83}MoS_2$ to re-established the $MoS_2$ phase, while the $Zn^{2+}$ gained the electron to deposit on the anode.

## Conclusions

In summary, $MoS_2$ nanosheets were successfully vertically grown on monodisperse MXene composites through a one-step hydrothermal method. The electronical conductivity and hydrophilicity in electrolyte of the composite were effectively improved compared with unmodified $MoS_2$. Meanwhile, the self-aggregation of $MoS_2$ and volume expansion during the charge/discharge reaction were significantly suppressed, resulting in excellent electrochemical properties with fast reaction kinetics. As a result, the $MoS_2/Ti_3C_2T_x$ cathode demonstrated discharge specific capacity of up to 277.8 mA h $g^{-1}$ at 0.1 A $g^{-1}$ and the capacity retention of 80% after 5000 cycles when the current density was 10.0 A $g^{-1}$. This work provided more possibilities for improving the electrochemical performance of energy storage layered materials.

## Author contributions

W. Su contributed to most experimental work. M. Lang completed the required experiments in the revised manuscript. Q. Zhang and Y. Yang assisted in characterization of some materials. H. Li conceived this idea and wrote the manuscript. F. Zhang conceived this idea and supervised the work. All the authors assisted in experiments and provided constructive comments on the text.

## Conflicts of interest

There are no conflicts of interest.

## Acknowledgements

This work is supported by The National Natural Science Foundation of China (22076122 and 52203269), The Shanghai Sailing Program (No. 20YF1435100), and Shanghai Government (22ZR1480200, 19SG42).

## References

1 X. Jia, C. Liu, Z. G. Neale, J. Yang and G. Cao, *Chem. Rev.*, 2020, **120**, 7795–7866.
2 W. S. V. Lee, T. Xiong, X. Wang and J. Xue, *Small Methods*, 2021, **5**, 2000815.
3 L. Cao, D. Li, T. Deng, Q. Li and C. Wang, *Angew. Chem., Int. Ed.*, 2020, **132**, 19454–19458.
4 Y. Li, Z. Wang, Y. Cai, M. Pam, Y. Yang, D. Zhang, Y. Wang and S. Huang, *Energy Environ. Mater.*, 2022, **5**, 823–851.
5 T. Wang, C. Li, X. Xie, B. Lu, Z. He, S. Liang and J. Zhou, *ACS Nano*, 2020, **14**, 16321–16347.
6 D. Kundu, B. D. Adams, V. Duffort, S. H. Vajargah and L. F. Nazar, *Nat. Energy*, 2016, **1**, 1–8.
7 H. Li, L. Ma, C. Han, Z. Wang, Z. Liu, Z. Tang and C. Zhi, *Nano Energy*, 2019, **62**, 550–587.
8 A. Kanwade, S. Gupta, A. Kankane, M. K. Tiwari, A. Srivastava, J. A. K. Satrughna, S. C. Yadav and P. M. Shirage, *RSC Adv.*, 2022, **12**, 23284–23310.
9 S. Luo, L. Xie, F. Han, W. Wei, Y. Huang, H. Zhang, M. Zhu, O. G. Schmidt and L. Wang, *Adv. Funct. Mater.*, 2019, **29**, 1901336.
10 Z. Yuan, L. Wang, D. Li, J. Cao and W. Han, *ACS Nano*, 2021, **15**, 7439–7450.
11 N. Zhang, X. Chen, M. Yu, Z. Niu, F. Cheng and J. Chen, *Chem. Soc. Rev.*, 2020, **49**, 4203–4219.
12 N. Guo, W. Huo, X. Dong, Z. Sun, Y. Lu, X. Wu, L. Dai, L. Wang, H. Lin, H. Liu, H. Liang, Z. He and Q. Zhang, *Small Methods*, 2022, **6**, 2200597.
13 Y. Shi, Y. Chen, L. Shi, K. Wang, B. Wang, L. Li, Y. Ma, Y. Li, Z. Sun and W. Ali, *Small*, 2020, **16**, 2000730.
14 S. Li, S. Zhang, T. Feng, H. Zhou and M. Wu, *RSC Adv.*, 2022, **12**, 18466–18474.
15 S. Li, Y. Liu, X. Zhao, K. Cui, Q. Shen, P. Li, X. Qu and L. Jiao, *Angew. Chem., Int. Ed.*, 2021, **60**, 20286–20293.
16 M. Wu, G. Zhang, H. Yang, X. Liu, M. Dubois, M. A. Gauthier and S. Sun, *InfoMat*, 2022, **4**, e12265.
17 N. Subjalearndee, N. He, H. Cheng, P. Tesatchabut, P. Eiamlamai, P. Limthongkul, V. Intasanta, W. Gao and X. Zhang, *Adv. Fiber Mater.*, 2022, **4**, 457–474.
18 J. Xu, Y. Liu, P. Chen, A. Wang, K.-j. Huang, L. Fang and X. Wu, *J. Colloid Interface Sci.*, 2022, **620**, 119–126.
19 J. Xu, S. Zhang, Z. Wei, W. Yan, X. Wei and K. Huang, *J. Colloid Interface Sci.*, 2021, **585**, 12–19.
20 F. Zhang, M. Du, Z. Miao, H. Li, W. Dong, Y. Sang, H. Jiang, W. Li, H. Liu and S. Wang, *InfoMat*, 2022, **4**, e12346.
21 L. Wang, X. Tan, Q. Zhu, Z. Dong, X. Wu, K. Huang and J. Xu, *J. Power Sources*, 2022, **518**, 230747.
22 H. Jia, K. Liu, Y. Lam, B. Tawiah, J. H. Xin, W. Nie and S.-X. Jiang, *Adv. Fiber Mater.*, 2023, **5**, 36–58.
23 J. Song, K. Xu, N. Liu, D. Reed and X. Li, *Mater. Today*, 2021, **45**, 191–212.
24 L. Ma, M. A. Schroeder, O. Borodin, T. P. Pollard, M. S. Ding, C. Wang and K. Xu, *Nat. Energy*, 2020, **5**, 743–749.
25 X. Yao, C. Li, R. Xiao, J. Li, H. Yang, J. Deng and M. S. Balogun, *Small*, 2022, **18**, 2204534.
26 X. Wu, X. Xie, H. Zhang and K.-J. Huang, *J. Colloid Interface Sci.*, 2021, **595**, 43–50.
27 J. Xu, Q. Liu, Z. Dong, L. Wang, X. Xie, Y. Jiang, Z. Wei, Y. Gao, Y. Zhang and K. Huang, *ACS Appl. Mater. Interfaces*, 2021, **13**, 54974–54980.
28 X. Geng, Y. Jiao, Y. Han, A. Mukhopadhyay, L. Yang and H. Zhu, *Adv. Funct. Mater.*, 2017, **27**, 1702998.
29 H. Sun, H. Liu, Z. Hou, R. Zhou, X. Liu and J.-G. Wang, *Chem. Eng. J.*, 2020, **387**, 124204.
30 J. Xu, Z. Dong, K. Huang, L. Wang, Z. Wei, L. Yu and X. Wu, *Scr. Mater.*, 2022, **209**, 114368.
31 M. Huang, Y. Mai, G. Fan, X. Liang, Z. Fang and X. Jie, *J. Alloys Compd.*, 2021, **871**, 159541.
32 H. Liu, J.-G. Wang, W. Hua, Z. You, Z. Hou, J. Yang, C. Wei and F. Kang, *Energy Storage Mater.*, 2021, **35**, 731–738.
33 J. Liu, N. Gong, W. Peng, Y. Li, F. Zhang and X. Fan, *Chem. Eng. J.*, 2022, **428**, 130981.
34 C. Li, C. Liu, Y. Wang, Y. Lu, L. Zhu and T. Sun, *Energy Storage Mater.*, 2022, **49**, 144–152.
35 W. Xu, C. Sun, K. Zhao, X. Cheng, S. Rawal, Y. Xu and Y. Wang, *Energy Storage Mater.*, 2019, **16**, 527–534.
36 S. Li, Y. Liu, X. Zhao, K. Cui, Q. Shen, P. Li, X. Qu and L. Jiao, *Angew. Chem., Int. Ed.*, 2021, **133**, 20448–20455.
37 M. Huang, Y. Mai, L. Zhao, X. Liang, Z. Fang and X. Jie, *Electrochim. Acta*, 2021, **388**, 138624.
38 Y. Dong, H. Shi and Z. S. Wu, *Adv. Funct. Mater.*, 2020, **30**, 2000706.
39 R. Zhao, A. Elzatahry, D. Chao and D. Zhao, *Matter*, 2022, **5**, 8–10.
40 X. Tang, X. Guo, W. Wu and G. Wang, *Adv. Energy Mater.*, 2018, **8**, 1801897.
41 F. Ming, H. Liang, G. Huang, Z. Bayhan and H. N. Alshareef, *Adv. Mater.*, 2021, **33**, 2004039.
42 Y. An, Y. Tian, J. Feng and Y. Qian, *Mater. Today*, 2022, **52**, 146–179.
43 Q. Zhang, H. Lai, R. Fan, P. Ji, X. Fu and H. Li, *ACS Nano*, 2021, **15**, 5249–5262.
44 S. Li, Y. Liu, X. Zhao, Q. Shen, W. Zhao, Q. Tan, N. Zhang, P. Li, L. Jiao and X. Qu, *Adv. Mater.*, 2021, **33**, 2007480.
45 M. Huang, Y. Mai, L. Zhao, X. Liang, Z. Fang and X. Jie, *ChemElectroChem*, 2020, **7**, 4218–4223.
46 J. Liu, P. Xu, J. Liang, H. Liu, W. Peng, Y. Li, F. Zhang and X. Fan, *Chem. Eng. J.*, 2020, **389**, 124405.
47 Z. Zhang, W. Li, R. Wang, H. Li, J. Yan, Q. Jin, P. Feng, K. Wang and K. Jiang, *J. Alloys Compd.*, 2021, **872**, 159599.
48 Y.-T. Wang, Z.-Z. Zhang and M.-X. Li, *Nano Futures*, 2022, **6**, 025001.
49 L. Liu, W. Yang, H. Chen, X. Chen, K. Zhang, Q. Zeng, S. Lei, J. Huang, S. Li and S. Peng, *Electrochim. Acta*, 2022, **410**, 140016.

50 P. Cao, N. Chen, W. Tang, Y. Liu, Y. Xia, Z. Wu, F. Li, Y. Liu and A. Sun, *J. Alloy and Compd.*, 2022, **898**, 162854.
51 Z. Sheng, P. Qi, Y. Lu, G. Liu, M. Chen, X. Gan, Y. Qin, K. Hao and Y. Tang, *ACS Appl. Mater. Interfaces*, 2021, **13**, 34495–34506.
52 Y. Q. Jin, H. Chen, L. Peng, Z. Chen, L. Cheng, J. Song, H. Zhang, J. Chen, F. Xie, Y. Jin, J. Shi and H. Meng, *Chem. Eng. J.*, 2021, **416**, 127704.
53 H. Jia, M. Qiu, B. Tawiah, H. Liu and S. Fu, *Compos. Commun.*, 2021, **27**, 100841.
54 Z. Yao, W. Zhang, X. Ren, Y. Yin, Y. Zhao, Z. Ren, Y. Sun, Q. Lei, J. Wang, L. Wang, T. Ji, P. Huai, W. Wen, X. Li, D. Zhu and R. Tai, *ACS Nano*, 2022, **16**, 12095–12106.